Acta Materialia 135 (2017) 411–421

Contents lists available at ScienceDirect

Acta Materialia

journal homepage: www.elsevier.com/locate/actamat

Full length article

Experimentally quantifying critical stresses associated with basal slip and twinning in magnesium using micropillars

Y. Liu [a], N. Li [b], M. Arul Kumar [a], S. Pathak [b, c], J. Wang [d, *], R.J. McCabe [a], N.A. Mara [b, e], C.N. Tomé [a, **]

[a] Materials Science and Technology Division, Los Alamos National Laboratory, Los Alamos, NM, 87545, USA
[b] Center for Integrated Nanotechnologies, Los Alamos National Laboratory, Los Alamos, NM, 87545, USA
[c] Chemical and Materials Engineering, University of Nevada, Reno, NV, 89512, USA
[d] Department of Mechanical and Materials Engineering, University of Nebraska-Lincoln, Lincoln, NE 68583, USA
[e] Institute for Materials Science, Los Alamos National Laboratory, Los Alamos, NM, 87545, USA

ARTICLE INFO

Article history:
Received 23 March 2017
Received in revised form
16 May 2017
Accepted 5 June 2017
Available online 7 June 2017

Keywords:
Magnesium
Micropillar compression
Basal slip
Twin

ABSTRACT

Basal slip and {01$\bar{1}$2} twinning are two major plastic deformation mechanisms in hexagonal closed-packed magnesium. Here we quantify the critical stresses associated with basal slip and twinning in single-crystal and bi-crystal magnesium samples by performing *in situ* compression of micropillars with different diameters in a scanning electron microscope. The micropillars are designed to favor either slip or twinning under uniaxial compression. Compression tests imply a negligible size effect related to basal slip and twinning as pillar diameter is greater than 10 μm. The critical resolved shear stresses are deduced to be 29 MPa for twinning and 6 MPa for basal slip from a series of micropillar compression tests. Employing full-field elasto-visco-plastic simulations, we further interpret the experimental observations in terms of the local stress distribution associated with multiple twinning, twin nucleation, and twin growth. Our simulation results suggest that the twinning features being studied should not be close to the top surface of the micropillar because of local stress perturbations induced by the hard indenter.

Published by Elsevier Ltd on behalf of Acta Materialia Inc.

1. Introduction

Magnesium (Mg) alloys have potential applications as structural components in the transportation industry due to their high strength-to-weight ratio [1]. Mg alloys have a hexagonal close-packed (hcp) structure and deform primarily via slip on the basal plane and {01$\bar{1}$2} tensile twinning [2–9]. Quantifying experimentally the critical stresses associated with basal slip and twinning (nucleation, growth and interactions) enables the prediction of the mechanical response of Mg and Mg alloys [10–19]. For example, recent cyclic studies reveal that twin junctions in single-crystal Mg have a considerable impact on the critical stresses necessary for twinning and detwinning, and can become a source of fracture [19–23]. However, these twinning phenomena and their effects on mechanical behavior are not well characterized or understood.

More than a decade ago, the micrometer-scaled pillar (micropillar) compression technique opened the possibility of exploring mechanical properties of sub-micron and micro-sized microstructural features owing to its relatively simple stress-states compared to other techniques such as micro/nano-indentation [24–29]. However, it is often observed that the mechanical strength increases with decreasing micropillar diameter, similar to the feature-size strengthening identified in nano-scale systems [30–38]. This so-called size-scale effect is related to the pillar surface-to-volume ratio. For face-centered cubic and body-centered cubic metallic materials, a micropillar manifests bulk mechanical behavior when the diameter is on the order of tens of microns [24,27]. For hcp metals such as Mg, several *in situ* electron and optical microscopy micropillar compression experiments have shown an obvious size-effect for {0001} basal slip compared with bulk single crystal results. Kelly and Hosford's plane-strain compression on single-crystal bulk Mg measured the compression yield stress for basal slip to be 4 MPa [39]. Yu et al. stated that the yield strength for basal slip could reach 2000 MPa when the

* Corresponding author.
** Corresponding author.
E-mail addresses: jianwang@unl.edu (J. Wang), tome@lanl.gov (C.N. Tomé).

http://dx.doi.org/10.1016/j.actamat.2017.06.008
1359-6454/Published by Elsevier Ltd on behalf of Acta Materialia Inc.

pillar diameter is smaller than 0.1 μm [40]. Ye et al. measured the yield strength for pillar diameters varying from 0.25 μm to 1.6 μm, and reported results in the range of 300 MPa to 50 MPa [41]. Moreover, *ex situ* micropillar compression results (the onset of yielding could not be determined) have provided some insights as well. Byer and Ramesh reported that the response of single-crystal Mg pillars oriented along (0001) are less sensitive to dislocation density when the pillar diameter increased to 10 μm [42]. Prasad et al. compared the size-effects of both basal slip and $\{01\bar{1}2\}$ twinning by compressing micropillars (3 μm) and macropillars (3 mm). These results indicate a significant size-effect for basal slip but a negligible size-effect for twinning [43].

In spite of these micropillar studies on single-crystal Mg, several important questions remain unanswered. First, what is the critical micropillar diameter that can reproduce similar yield strength for basal slip as the bulk single crystal counterpart? Second, what is the critical micropillar diameter associated with $\{01\bar{1}2\}$ twinning? Third, what are the critical stresses associated with basal slip and twinning? To address these issues, we employ *in situ* scanning electron microscopy (SEM) micropillar compression. We aim at quantifying the critical stresses associated with basal slip and twin growth (twin boundary migration). Twin nucleation could be identified but the corresponding nucleation stress is related to stochastic factors, especially local stress or strain concentration. Corresponding to these goals, we design micropillars with specific orientations and microstructures. The critical resolved shear stress (CRSS) values deduced here for a 10 μm pillar are: twin boundary migration (29 MPa) and basal slip (6 MPa). The CRSS ratio of twin growth and basal slip in this study is estimated as 5, which is the same as Kelly & Hosford plane-strain compression results and comparable to various bulk measurements in the range of 2.5–4.4 in the literature [7]. The use of local plasticity simulations provides us with insight about the non-homogeneous stress field inside the pillar and allows us to understand the correlation between the micropillar test conditions and the observed twinning configurations in terms of local stress fields.

2. Experimental details

Mg single crystals were grown using the Bridgman method and $\{01\bar{1}2\}$ deformation twins were introduced by pre-loading in tension along the c-axis to a total strain of 1%. Standard metallographic techniques were used to polish specimens. A solution of 10% HNO_3 and 90% H_2O was used to chemically polish each specimen to remove any residual surface damage. An FEI XL30 with an accelerating voltage of 25 kV was used for electron backscatter diffraction (EBSD) to obtain crystal orientation for both parent and twin phases. An FEI Helios 600 focused ion beam (FIB) with accelerating voltage 30 kV was used to prepare micropillars. The length and diameter of the micropillars were measured by FIB/SEM before and after straining. The length-to-diameter ratio was 2.5-to-1 and the taper angle is within 2-to-5°. Such geometrical dimensions ensure uniform deformation [27]. *In situ* SEM analyses were conducted on a FEI Magellan 400 and an FEI Helios 660 SEM with an accelerating voltage of 1–2 kV (The low kV in secondary electron mode allows better surface detail such as revealing slip steps.). *In situ* micropillar compression was performed using a Hysitron PI-85 and PI-85 × R SEM PicoIndenter. The micropillar compression tests were conducted with a 20 μm flat punch tip at a strain rate of $1 \times 10^{-3}s^{-1}$. During the *in situ* testing, the indenter was controlled to minimize the misalignment between the tip and the top surface of the pillars, and a minimum of 3 tests were performed for each type of pillar to ensure the reproducibility of results. All of the micropillars were compressed to a maximum of 10% of the pillar height and no *ex situ* compression was performed. We plotted stress-strain curves to show mechanical response. The stress was calculated by using a full width at half maximum (FWHM) approach [44], where the diameter in the middle of the pillar is estimated from known (1) top surface diameter, (2) taper angle and (3) total length of the pillar. The strain was estimated by displacement/height of the pillar. The displacement is considered once the indenter contacts the pillar. Postmortem transmission electron microscope (TEM) specimens were prepared using an FEI DB235 dual-beam FIB with an accelerating voltage of 30 kV. An FEI Tecnai F30 field emission transmission electron microscope with accelerating voltage of 300 kV was used for TEM imaging.

3. Results and discussion

3.1. Micropillar design

Micropillar compression experiments were performed along $<2\bar{1}\bar{1}3>$ (basal slip favored) and $<10\bar{1}0>$ (twinning favored) orientation in single-crystal Mg, and also in bi-crystals that consist of the previous parent orientation and a $\{01\bar{1}2\}$ twin. Fig. 1 shows EBSD images of pre-strained samples and reveals the crystal orientation of both the single-crystal pillars (1 and 3) and bi-crystal pillars (2 and 4). The three-dimensional (3D) geometry of the four micropillars (1–4) determined from the EBSD analysis is schematically illustrated in Fig. 2, together with the maximum Schmid factors for basal slip (m_b) and twinning (m_t). Based on the Schmid factors, pillars 1 and 2 favor basal slip while pillars 3 and 4 favor twinning.

3.2. Micropillars with 10 μm diameter reproduce bulk single crystal values

By varying the diameter of pillar 1 (basal slip preferred single-crystal pillar with m_b~0.49), we deduce that the minimum diameter necessary to obtain a similar yield strength for basal slip to bulk Mg single crystal with similar m_b is 10 μm. Fig. 3a shows an undeformed micropillar with slight tapering (the diameter difference between the top surface and the base is less than 5%). The height of all pillars is about 2.5 times the pillar diameter in order to avoid barreling or buckling effects [27]. Postmortem SEM images of pillar 1 with diameters of 3 μm (Fig. 3b), 5 μm (Fig. 3c) and 10 μm (Fig. 3d) reveal that obvious basal slip occurs at the upper edge of these micropillars, and that it is repeatable. Fig. 3e compares the stress-strain curves of these micropillars and shows multiple stress-drops corresponding to multiple events of basal slip. The elastic slope is affected by incomplete contact of the indenter with the top of the pillar during the initial loading. The taper angle is within 2–5°. The true stress was estimated using the FWHM approach. The *in situ* nature of the experiment allows us to directly correlate a discrete slip event with the corresponding load. We thus directly calculate the local resolved shear stress for the slip event at the corresponding load value (given by the *in situ* movie and snapshots). The corresponding stress is marked by stars on each curve in Fig. 3e. We determine the yield strength both when the stress starts to deviate unambiguously from linearity and when slip traces are detected. The yield strength for these micropillars manifests a clear size-effect. Pillars with smaller diameter exhibit higher onset yield strength. By comparing with literature results for both *ex situ* and *in situ* pillar compression with similar m_b, we determine the critical size that represents the mechanical responses of bulk Mg. Fig. 3f (compared to *ex situ* literature) shows the measured flow stress as a function of pillar diameter compares well with *ex situ* micropillar compression with similar pillar diameters [42]. Fig. 3g (compared to *in situ* literature) shows the comparison of the onset yield strength as a function of pillar diameter with other *in situ*

transmission electron and optical microscopy compression results [39,41]. We conclude that the micropillar with 10 μm diameter from the present study well represents average bulk value for the onset of basal slip.

It must be pointed out that the CRSSs associated with both prismatic and pyramidal slip are an order of magnitude higher than basal slip for Mg. It is extremely difficult to experimentally activate these slip events. Even for <0001>-oriented single-crystal Mg, basal slip can be activated though m_b is nearly zero. This phenomenon is attributed to surface damage, slight misalignment, indenter friction, etc [42]. Consequently, we did not study the critical size for prismatic and pyramidal slip in micropillar experiments. However, it is doable to measure the critical stress associated with twin growth using micropillar tests. When the sample is compressed along the direction perpendicular to the basal axis, $\{01\bar{1}2\}$ twinning can be activated while the corresponding Schmid factor associated with basal slip is close to zero. In addition, mechanical tests for bulk Mg samples showed a relatively low CRSS associated with $\{01\bar{1}2\}$ twinning. Compared to the study of basal slip, micropillar studies of twinning as a function of pillar diameter are limited. Prasad et al. reported that the stress plateaus for $\{01\bar{1}2\}$ twinning of both micropillars (3 μm) and macropillars (3 mm) are comparable and around 40 MPa. However, the 3 μm micropillar data exhibits a stress spike (150 MPa) prior to the plateau, which is attributed to twin nucleation from the free surface [43]. In addition, Yu et al. reported an ultra-high twin nucleation stress of 800 MPa when the pillar diameter is smaller than 0.1 μm [45]. On the other hand, Liu et al. reported a lower nucleation stress of ~280 MPa when dog-bone shaped micro/nano-pillars were tested in tension along <0001> [9]. These results indicate that the stress corresponding to twin nucleation is influenced by uncertain factors (in other words, local stress/strain concentration). Thus, we focused on the CRSS associated with twin growth or twin boundary migration.

By varying the diameter of pillar 3 (single-crystal pillar that favors twinning; m_t~0.49), we found that 10 μm diameter micropillar gives a similar stress plateau associated with twin boundary migration as bulk Mg single crystals with similar m_t. Fig. 4a presents SEM micrographs of undeformed and deformed/twinned 5 μm diameter single-crystal micropillars that favor twinning (pillar 3). Twinning occurs at ~60 MPa, corresponding to a significant stress drop at a strain of 0.02. The stress-plateau, ~60 MPa, remains for the strain range 0.02–0.05, corresponding to twin boundary migration. As a consequence, the pillar diameter expands by a measurable 5–6%. Similar phenomena have been observed in other pillars (details can be found in Supplementary Movie 1). The stress-strain curves of micropillars with 3 μm, 5 μm and 10 μm diameter in Fig. 4b show the first obvious stress drop (corresponding to twin nucleation), and stress-plateau after that (corresponding to twin boundary migration). The critical compression stress to activate twin in Fig. 4c shows almost negligible size-effect. Most importantly, the CRSS associated with twin boundary migration does not show obvious size-effect when micropillars have several micrometers diameter. It is worth mentioning that twin growth stress did show size-effect as demonstrated in nanopillar tests [9]. This size effect was attributed to the change in twinning mechanisms [46–48]. As a consequence, our study demonstrates that 10 μm diameter micropillar can be used to characterize mechanical behavior of bulk Mg as far as basal slip and twinning are concerned.

Supplementary video related to this article can be found at http://dx.doi.org/10.1016/j.actamat.2017.06.008.

3.3. Basal slip at 12 MPa (m_b~0.49)

Fig. 5 presents *in situ* micropillar compression on pillar 2 with a 10 μm diameter manifesting the onset compressive stress of 12 MPa for basal slip activation. A postmortem SEM image of pillar 2 (Fig. 5a) reveals multiple basal slip events in the middle of the pillar due to the confinement of the pre-existing twin in the upper part of the pillar. No obvious migration of the twin boundary (marked by white dash-lines) occurs during the deformation as is evident by comparing the before (Fig. 5b) and after (Fig. 5c). Compared to Fig. 5a, the SEM view in Fig. 5b–c is rotated 90° clockwise in order to better image the location of the pre-existing twin. As shown in Fig. 5d–e, the onset compressive yield stress for basal slip (manifested by multiple stress-drops) of pillar 2 is 12 MPa, similar to the one of single crystal pillar 1. (Fig. 5d is re-plotted from Fig. 3e). Details of the formation of basal slip can be found in sequential *in*

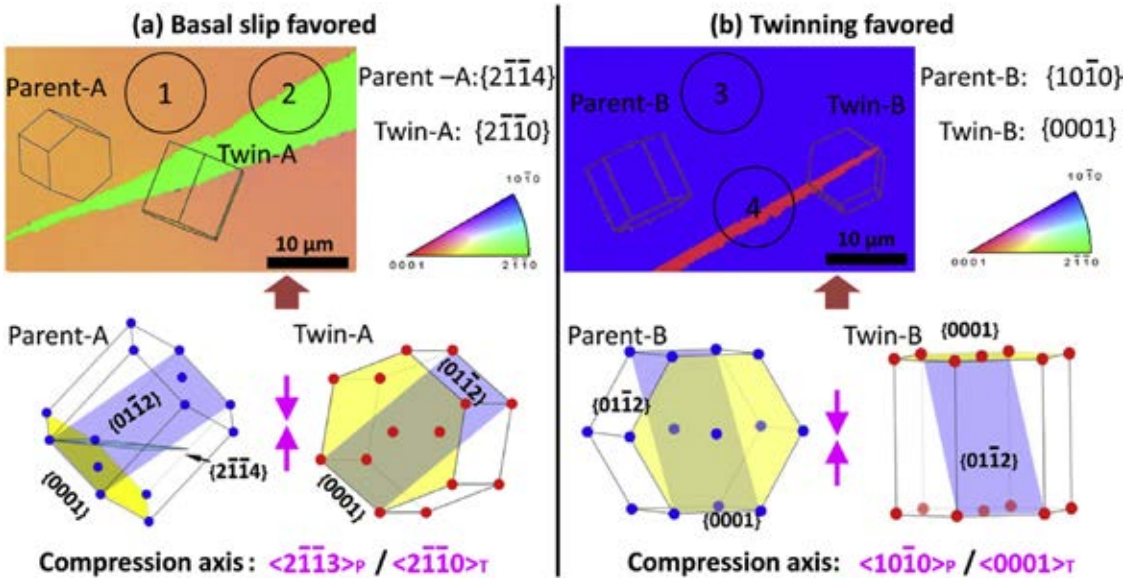

Fig. 1. Micropillars are designed to favor (a) basal slip and (b) twinning, respectively. The single-crystal and bi-crystal counterpart with a $\{01\bar{1}2\}$ twin are examined in this study. EBSD images of samples' top surface and the corresponding crystal structure observed from the side view of the micropillars are presented.

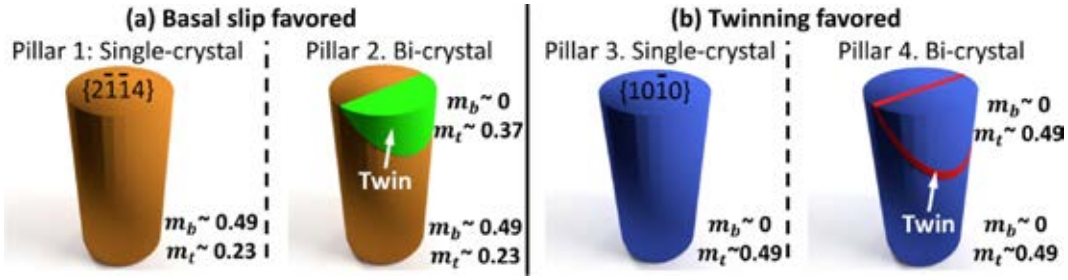

Fig. 2. The structure and geometry of (a) basal slip and (b) twinning favored micropillars. Maximum Schmid factors of each variant for basal slip (m_b) and twinning (m_t) are shown.

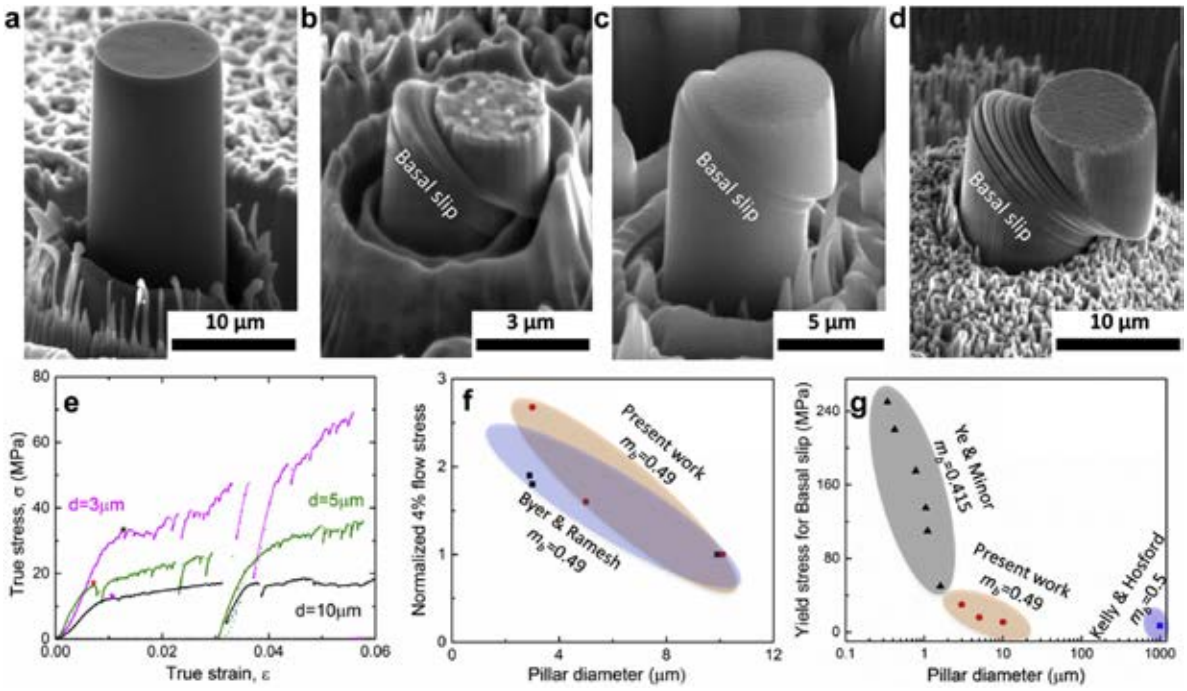

Fig. 3. (a) An SEM micrograph of an un-deformed micropillar. SEM micrographs of deformed single-crystal pillars that favor basal slip (pillar 1) with diameters (b) 3 μm, (c) 5 μm and (d) 10 μm reveal the activation of basal slip all from the edge of the top surface. (e) The stress-strain curve is estimated by FWHM approach, while the star on each curve represent the direct estimation of the critical stress to activate a discrete slip event along with *in situ* movies and corresponding load values. The yield strength of these micropillars reveals an obvious size-effect for basal slip, manifested by multiple stress-drops. By comparing with literature results on pillar diameter as a function of (f) *ex situ* 4% flow stress [42] and (g) *in situ* onset yield stress [39,41], the micropillar with 10 μm diameter from the present study is considered to represent the mechanical responses of bulk Mg.

situ SEM snapshots in Figs. 6 and 7. During the *in situ* compression experiment the maximum viewing angle is 25° and the rim of the crater prevents the viewing of the base. Therefore, the *in situ* snapshots do not show the base due to the narrow width of the trench. To overcome this limitation, the length and diameter are measured by FIB/SEM before and after straining. Basal slip (indicated by orange arrows) takes place in both the single-crystal pillar 1 as shown in Fig. 6 (details can be found in Supplementary Movie 2) and bi-crystal pillar 2 with the pre-existing twin boundary marked in white dash lines in Fig. 7 (details can be found in Supplementary Movie 3). Furthermore, postmortem bright field TEM and select area diffraction (SAD) results on pillar 1 confirm basal slip activity, as shown in Fig. 6d. We did not observe the twin boundary (marked by white dash-lines) migrate during compression of the bi-crystal pillar (Fig. 7). The major plastic deformation is associated with basal slip. In addition, the geometry of the parent/twin in the bicrystal allows for basal slip to occur within the parent without the basal dislocation needing to interact with the twin boundary, essentially giving single crystal behavior.

Supplementary video related to this article can be found at http://dx.doi.org/10.1016/j.actamat.2017.06.008.

3.4. Twin growth at 60 MPa (m_t ~ 0.49)

Most of the volume of pillar 3 and pillar 4 with 10 μm diameters has been completely twinned after compression, as shown by the postmortem SEM image of pillar 3 in Fig. 8a. Twin nucleation and twin boundary migration events can be found in both of these tests. The stress-strain curve in Fig. 8b shows twin nucleation from the free surface in pillar 3 at a higher stress (116 MPa) accompanied by a large stress-drop. Besides the twin nucleation in pillar 3, both pillar 3 (Fig. 8b) and pillar 4 (Fig. 8c) reveal similar stress plateaus at 60 MPa with multiple small magnitude stress-drops, corresponding to the twin growth or twin boundary migration that are evidenced by *in situ* snapshots in Figs. 9 and 10. Furthermore, postmortem bright field TEM and SAD results on the single-crystal pillar 3 in Fig. 8d confirm the formation of $\{01\bar{1}2\}$ twins.

Sequential *in situ* SEM snapshots reveal the twin nucleation and twin boundary migration in pillar 3 in Fig. 9 (details can be found in Supplementary Movie 4) and pillar 4 in Fig. 10 (details can be found

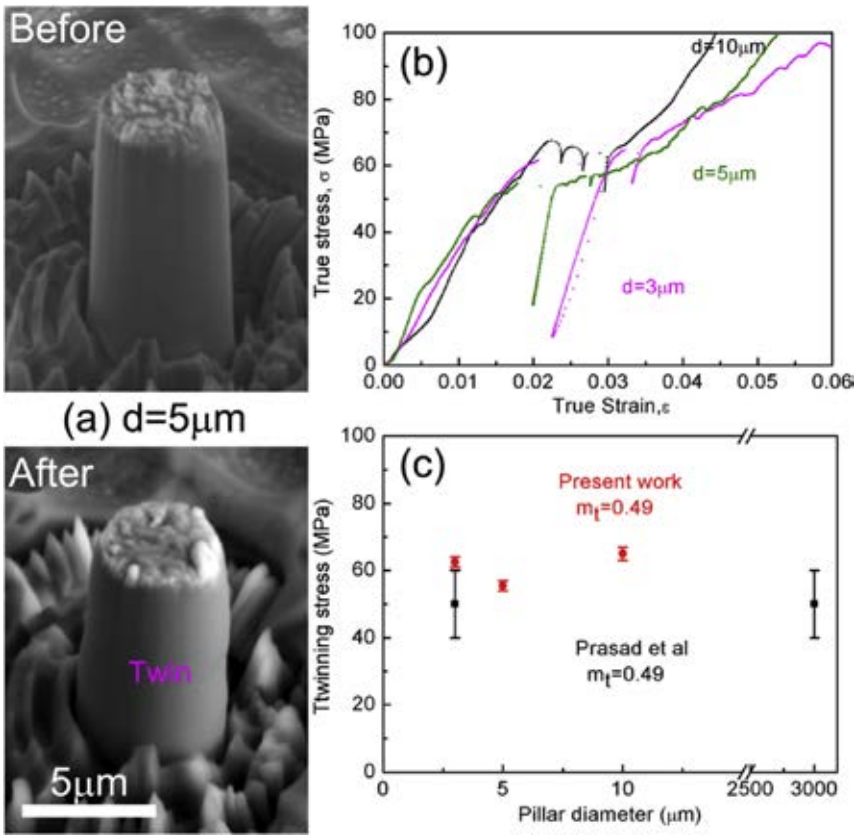

Fig. 4. (a) SEM micrographs of undeformed and fully twinned single-crystal micropillars of 5 μm diameter that favor twinning (pillar 3). Twinning occurs at ~60 MPa, corresponding to a significant stress drop at a strain of 0.02. The stress-plateau, ~60 MPa, remains for the strain range 0.02–0.05, corresponding to twin boundary migration. As a consequence, the pillar diameter expands about 5–6%. (Details can be found in Supplementary Movie 1). Similar phenomena have been observed in other pillars. (b) The stress-strain curves of micropillars with 3 μm, 5 μm and 10 μm diameter are estimated by FWHM approach. The stress-plateaus start when the top of these micropillars start expanding, indicating the activation of twinning. (c) Comparison of twinning stress, showing a negligible size-effect.

in Supplementary Movie 5). For pillar 3, two fine twins (with average thickness ~ 1 μm) nucleate and traverse the pillar as shown in Fig. 9b (white and orange dash-lines indicate the lower boundary of the two twins). The lower twin continuously grows to lower left of the pillar at the applied stress plateau of ~60 MPa. Fig. 9c–d shows a migration of the lower twin boundary by about 2 μm and 5 μm, respectively. During this process, the upper twin (marked in white) remains stable and does not grow, a feature that will be discussed and explained in the following section. For pillar 4, similar stress plateaus and multiple small stress-drops were observed, corresponding to jerky twin boundary migration. A new twin nucleates (marked by orange dash-lines) below the pre-existing twin (marked by white dash-lines) at 63s (Fig. 10b), and the boundary continues migrating towards the lower left (Fig. 10c–d). The applied compressive stress for twin growth is estimated to be 60 MPa (~29 MPa for the RSS) regardless of the presence of a pre-existing twin. During this process, the upper pre-existing twin (marked in white) remains stable and does not grow.

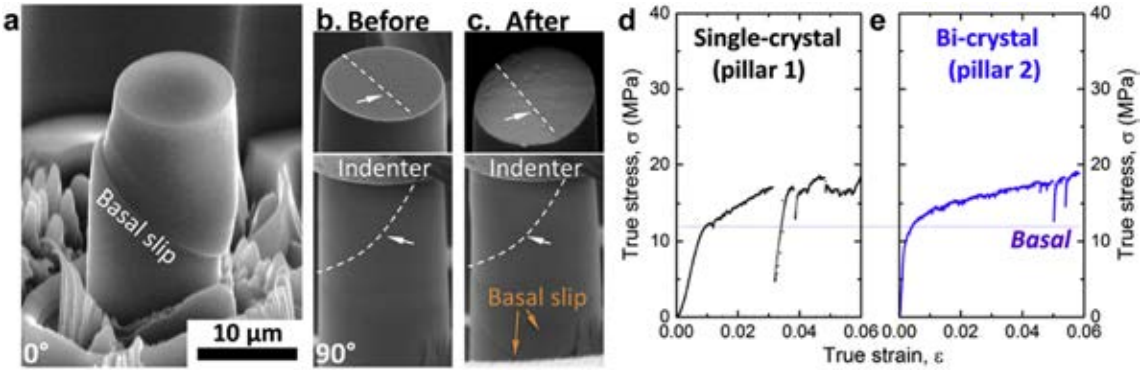

Fig. 5. (a) The deformed bi-crystal pillars that favor basal slip (pillar 2) with 10 μm diameter reveals the activation of basal slip from the middle of the pillar. The surface and the side view of the pillar (b) before and (c) after the deformation manifest no migration of the pre-existing twin boundary (marked by white dash-lines). The similar yield strength (12 MPa) of (d) pillar 1 and (e) pillar 2 with 10 μm diameter confirm the critical stress for basal slip in spite of the pre-exiting twin domain that does not favor basal slip.

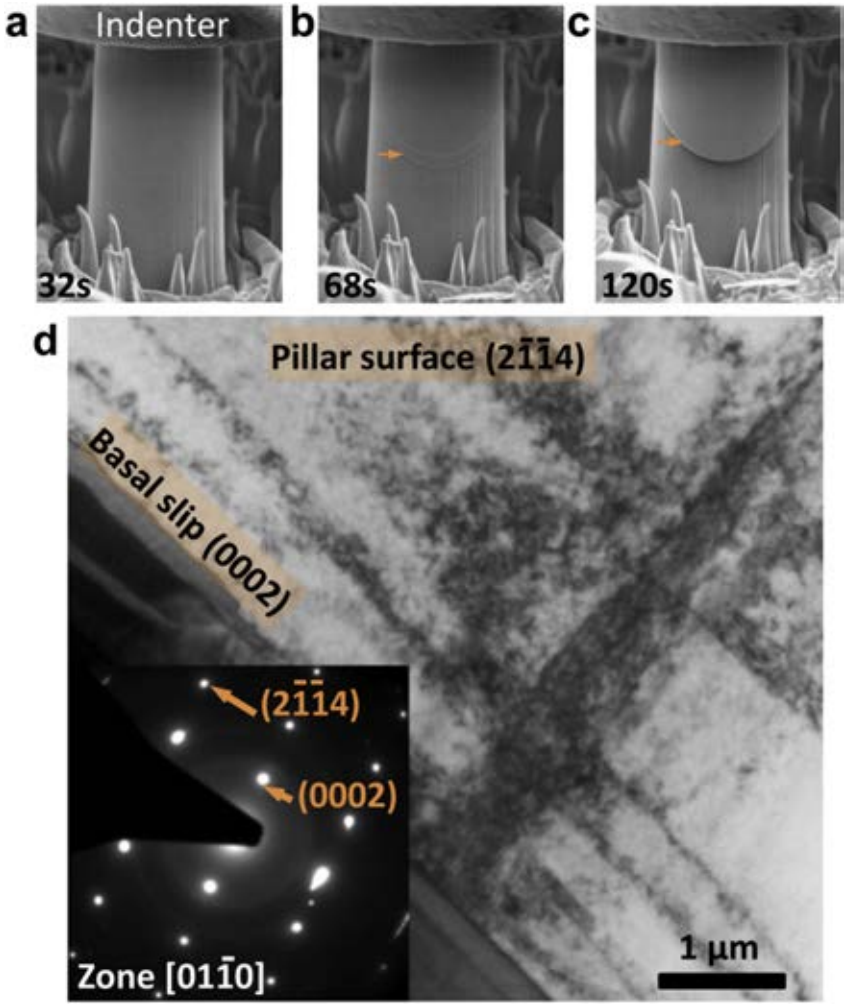

Fig. 6. (a–c) Sequential *in situ* SEM snapshots reveal basal slip (marked with orange arrows) in single-crystal pillar 1. The images at 32s, 68s, and 120s correspond to the true strain of 0.01, 0.03 and 0.07, respectively. Details can be found in Supplementary Movie 2. (d) Postmortem bright field TEM and inserted SAD confirm the basal slip in single-crystal pillar 1. (For interpretation of the references to colour in this figure legend, the reader is referred to the web version of this article.)

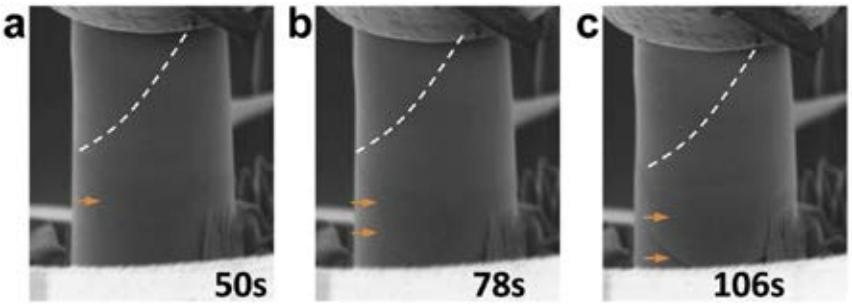

Fig. 7. (a–c) Sequential *in situ* SEM snapshot reveal basal slip (marked with orange arrows) in bi-crystal pillar 2 with the pre-existing twin boundary (marked in white dash lines). The images at 50s, 78s, and 106s correspond to the true strain of 0.02, 0.04 and 0.06, respectively. Details can be found in Supplementary Movie 3. No obvious twin boundary migration is observed in pillar 2. (For interpretation of the references to colour in this figure legend, the reader is referred to the web version of this article.)

Supplementary video related to this article can be found at http://dx.doi.org/10.1016/j.actamat.2017.06.008.

A clear size-effect for twin nucleation is evident when comparing the twin nucleation stress for a 10 μm pillar in this study (116 MPa) with the reported values of 160 MPa for compression testing of 3 μm pillar [43], 800 MPa for compression testing of 0.1 μm pillar [45], and 280 MPa for tension testing of 0.1–0.4 μm pillar [9]. On the other hand, the compressive stress for twin growth is relatively insensitive to the pillar size. The twin growth stress (60 MPa) for 10 μm micropillars in this study shows similar stress plateaus when compared to the ones of smaller micropillars (3 μm) and macropillars (3 mm), reported to be 30–50 MPa [43]. Furthermore, Kelly and Hosford's plane-strain compression on single-crystal bulk Mg revealed the CRSS for twinning to be 20 MPa [39] giving a CRSS twin/basal ratio of 5. Considering the measured compressive stresses for twin growth (60 MPa) and basal slip

(12 MPa) with corresponding Schmid factors in this study, our CRSS twin/basal ratio is the same as Kelly and Hosford's measurement and is comparable to the literature estimates in the range of 2.5–4.4 [7].

For both pillar 3 and pillar 4, similar stress plateaus and multiple small stress-drops during twin growth were observed regardless of the presence of a pre-existing twin boundary. Some interesting twinning characteristics have drawn our attention. Both pillars 3 and 4 contain two twins, but only the twin that is farthest away from both the indenter and the base exhibits continuous growth. Only pillar 3, without a pre-existing twin, presents a high nucleation stress from the free surface. Such evidence poses several questions: (1) are there any indenter effects on twinning characteristics? (2) Do pre-existing twins facilitate the nucleation of other twins? (3) Which circumstances favor heterogeneous twin growth during micropillar compression? In order to understand these unique twinning characteristics in particular, and to improve our interpretation of micropillar results related to twinning in general, we have employed a full-field elasto-visco-plastic Fast Fourier Transform (FFT) model to predicts the local stress distribution associated with our twinning configurations [49].

3.5. Indenter effects on twinning characteristics

We first discuss indenter effects on twin nucleation and growth. A schematic representation of the FFT model setup is shown in Fig. 11a–b, consisting of a Mg single grain with two hard phases bounding it at top and bottom of the unit cell, meant to represent the rigid flat diamond indenter and the pillar base, respectively. The unit cell is loaded by displacing the hard phase (indenter) in the simulation, and traction free conditions are enforced on the lateral surfaces. In order to study indenter effects, we have placed a twin in two different locations: in the first set of simulations, both twin tips end at the free surface (Fig. 11a) and in the second set of simulations one twin tip ends at the free surface and the other at the boundary with the hard phase (Fig. 11b). The position of the twin tip is characterized by the separation parameters 'g' and 'r' from the hard face and from the free surface, respectively.

For all of the simulations, the c-axis of the Mg grain is oriented perpendicular to the compression direction (y-direction). The imposed deformation and the twinning shear are accommodated elastically and plastically in the hcp Mg, and the diamond hard phase is assumed to only deform elastically. The plastic deformation of Mg is accommodated by basal, prismatic and pyramidal slip

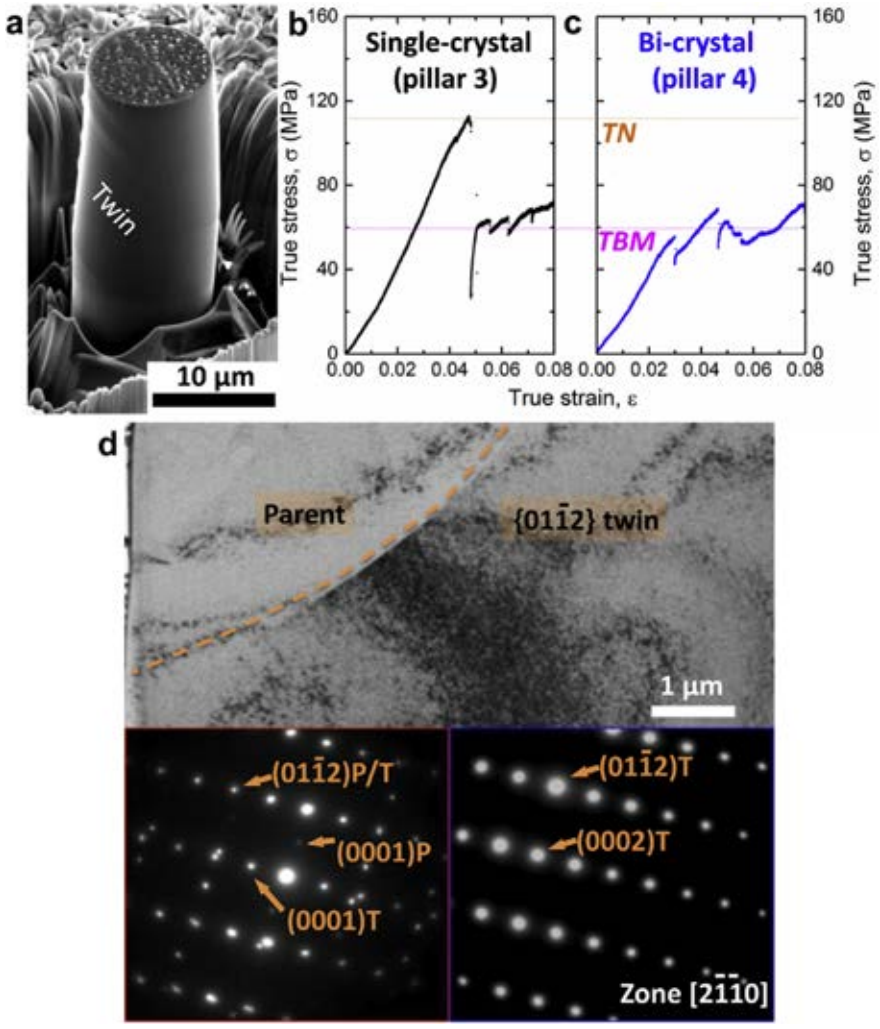

Fig. 8. Single-crystal (pillar 3) and bi-crystal (pillar 4) that favor twinning with 10 μm diameter shows that both pillars have nearly completely twinned after the compression. (a) A showcase of the deformed twinned pillar 3. The stress-strain curves of (b) pillar 3 and (c) pillar 4 both reveal the stress necessary for twin boundary migration is 60 MPa, regardless of the pre-exiting twin. The twin nucleation stress from the free surface in the single-crystal pillar 3 is 116 MPa. (d) Postmortem bright field TEM and inserted SAD confirm the {01$\bar{1}$2} twin relation in single-crystal pillar 3.

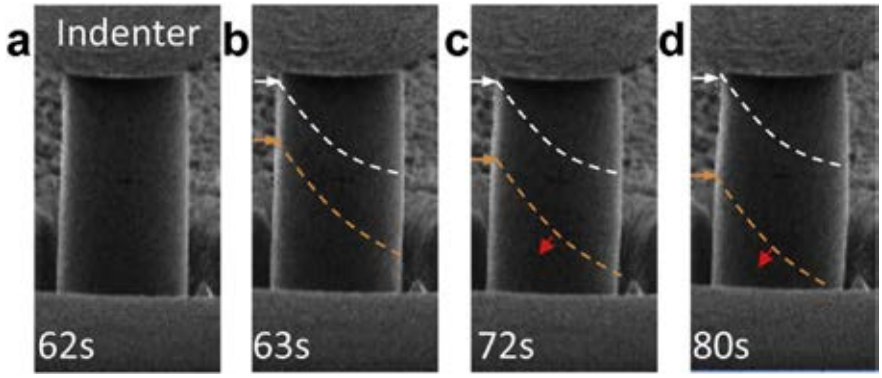

Fig. 9. Sequential *in situ* SEM snapshots reveal twin nucleation and growth in single-crystal pillar 3. The images at 62s, 72s, and 80s correspond to the true strain of 0.05, 0.06 and 0.07, respectively. Details can be found in Supplementary Movie 4. (a–b) Two fine twins nucleate (white and orange dash-lines indicate the lower boundary of the two twins) simultaneously from 62–63s. (c–d) The lower twin (marked by orange) continuously grows with twin boundary migrating to lower left of the pillar. During this process, the upper twin (marked in white) remains stable and does not migrate. (For interpretation of the references to colour in this figure legend, the reader is referred to the web version of this article.)

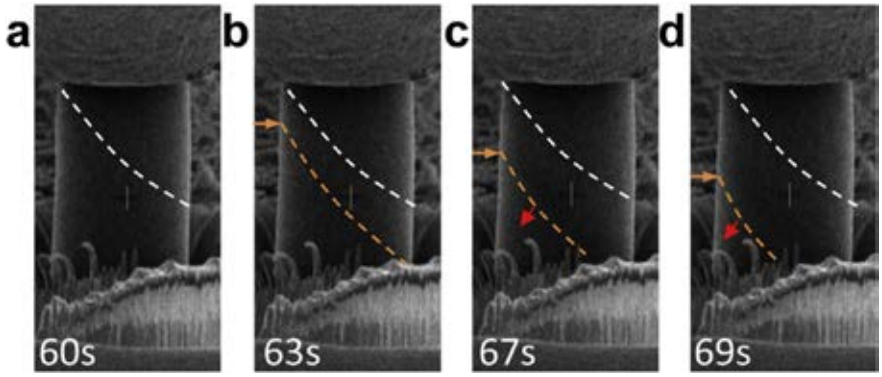

Fig. 10. Sequential *in situ* SEM snapshots reveal twin nucleation and growth in bi-crystal pillar 4 with a pre-existing narrow twin (marked in white dash lines). The images at 60s–69s correspond to the true strain of 0.05–0.06. Details can be found in Supplementary Movie 5. (a–b) A new twin nucleates below it (marked by orange dash-lines) and (c–d) grows towards the lower left, while the pre-existing twin (marked in white) remains stable and does not grow. (For interpretation of the references to colour in this figure legend, the reader is referred to the web version of this article.)

systems, and its anisotropic elastic constants and the critical resolved shear stresses are the same as in a previous study [49]. The hard phase deforms by isotropic elasticity with a Young's modulus of 1200 GPa and Poisson ratio of 0.2, corresponding to diamond. Since the simulations involve small strains, we do not account for lattice rotation or work hardening. The unit cell is discretized into $3 \times 500 \times 1500$ voxels including a 10 voxels thickness for the hard phase. The twin thickness in all the simulations is 9 voxels.

The FFT simulations of the numerical pillar experiments are done in the following sequence. Initially, the unit cell is subjected to compression along the z-direction, which gives a Schmid factor of ~0.49 for the $\{01\bar{1}2\}$ tensile twin. After reaching the twin resolved shear stress (TRSS) of ~20 MPa (CRSS value), the twin is introduced at a preselected region by first reorienting the crystal according to the twinning relationship and next by imposing the total twinning shear ($S = 0.129$) using 2000 small strain increments. As a consequence, the FFT calculations provide the local stress distribution in the unit cell under the indenter load, before and after twinning. To understand the role of the surrounding medium on twinning we calculate the average twin back-stress, which is the difference between the average TRSS in the twin after and before the twinning process. The twin back-stress is always negative and we present here the absolute value. The calculated back-stresses in the twin region for both the free and the 'hard' surface cases as a function of twin tips position are shown in Fig. 11c. The twin back-stress is practically not affected by the separation of the twin from the 'hard' surface 'g' in the free surface case. But in the hard surface case the twin back-stress is significantly affected depending on the position of the twin tip 'r'. It shows that if the shear at the twin tip is constrained by the hard phase, then a large back-stress is induced due to lack of plastic accommodation. By comparing the twin back-stress associated with each of these two cases we conclude that twin growth for twins intersecting the free surface is more likely than twin growth for twins entering in contact with the hard indenter surface.

In addition to the average stress in the twin, there is also a significant variation of TRSS along the twin interface. This dependence is similar to the results presented in Ref. [49] for both cases. Instead of showing the TRSS distribution everywhere in the twin, we present here the TRSS at the tip of the twin (averaged over the twin thickness) for the free surface case. The calculated average TRSS at the twin tip as a function of the twin tip position 'g' is shown in Fig. 11d. It can be seen that the average TRSS at twin tip A, which is far from the hard phase, does not vary with twin tip position. However, the average TRSS at twin tip B, which is closer to the hard phase, varies rapidly when the twin tip is close to the hard phase and experiences a larger back-stress (and so less TRSS). This is due to the perturbation of the stress field induced by the presence of the hard phase and its inability to accommodate plastic deformation. From this simulation results, we speculate on two

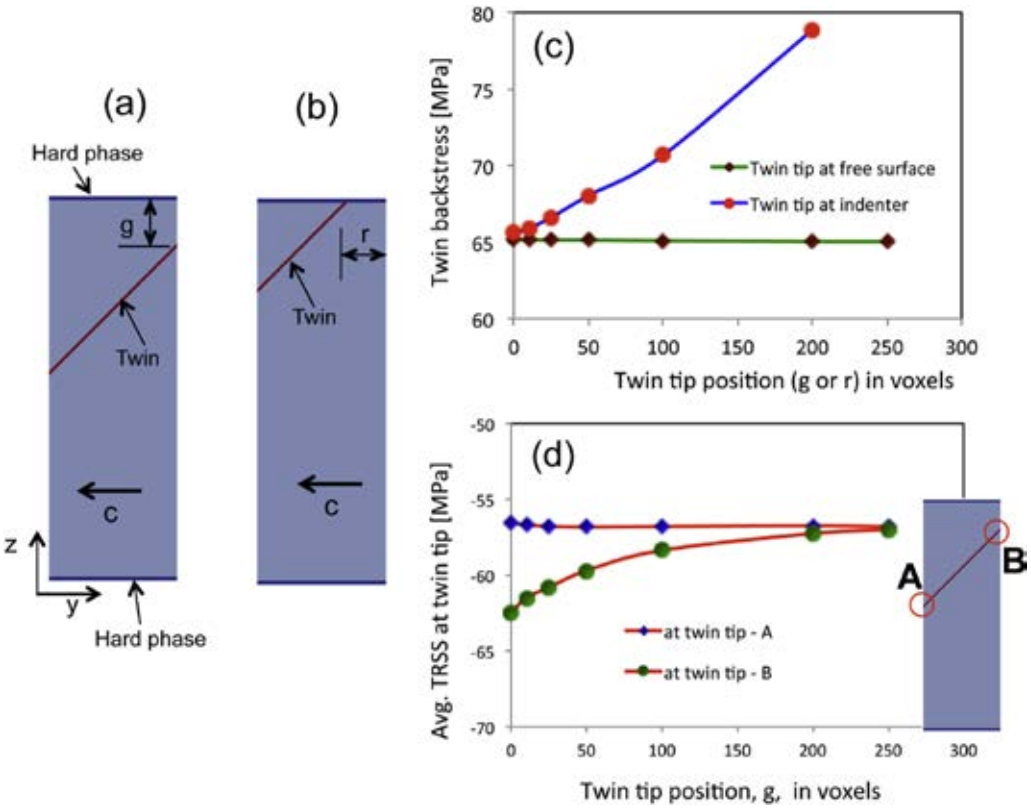

Fig. 11. Schematic representation of the FFT simulation setup with (a) both twin tips at the free surface and (b) one twin tip at free surface and another at the hard phase material. The hard phase represents the indenter with friction in the pillar experiments. The twin position is characterized by ***g*** for free surface case and ***r*** for hard phase case. (c) Average twin backstress for different positions with respect to the hard phase for both the free surface and hard phase case. (d) Average TRSS at both the twin tips for the free surface case. The average is performed in a small region in the twin at the tip with the region size of 9 voxels (same as twin thickness).

important points. First, the differences in the TRSS at the twin tips may lead to asymmetrical twin growth. Second, in the case of twins located close to the hard indenter, the indenter significantly affects the stress state by increasing the back-stress acting on the twin. As a consequence, characterizing the stress state associated with the activation of twinning or other twinning features, such as twin junctions, should be done at a position removed from the indenter or the base of the pillar, to avoid perturbations induced by the hard 'phases'.

3.6. Local stress analysis on various scenarios of twin nucleation or growth

In the micropillar experiments, we have observed the nucleation of new twins at the pillar free surface. Moreover, the twin nucleation stress is much higher in single-crystal pillar 3 compared to pillar 4 with a pre-existing twin. To understand and explain this feature we use the calculated stress distributions from the FFT simulations. In Fig. 12a–b, we show the TRSS distribution along the right pillar surface for both the free and the 'hard' surface cases. The TRSS distribution is nearly constant along the free surface for most of the region except at the interval spanned by the twin. In both cases we observe a stress reversal in the TRSS due to twinning shear accommodation, which is to be expected. At the same time, we have observed an unexpected and fascinating stress concentration at the pillar surface, which may facilitate new twin nucleation. This local stress concentration can be explained using simple classical mechanics. In Fig. 12c, we show schematically a twin inside a pillar with a free surface at both twin tips. The marked twinning shear associated with the twin (as shown in black arrows) is constrained by the fact that the friction with the indenter prevents the lateral displacement of the upper portion of the pillar. As a consequence the surrounding matrix imposes an opposite shear to the twin as shown in small red arrows in Fig. 12d and, then, to a shear stress reversal in the twin and its vicinity. In addition, the reaction forces induce a twisting moment about the out of plane direction which tends to 'bend' the pillar and creates the shear stress concentration at the twin free surface shown in the TRSS profile (Fig. 12a–b) from FFT calculations. This local stress concentration may help to nucleate another twin at the pillar surface, which is what we observe experimentally in pillar 3 and 4. In principle, we expect this process of twin nucleation and propagation to repeat itself at regular intervals.

Next, we analyze the case of two parallel twins present in a pillar, and investigate if they will grow similarly or differently. We have observed in pillar 4 that the lower twin (which is farther away from the hard indenter) grows, while the upper twin (in contact with the indenter) does not grow. Here we also employ FFT calculations with two twins to study their propensity for growth. The simulation setup with two twins is shown schematically in Fig. 13a. We have performed different simulations by varying the positions of the twins. One tip of the upper twin is always in contact with the 'hard' surface, while for the other twin the tips always terminate at the free surfaces. The position of the twin closer to the hard phase (twin-2) is varied with a parameter, *r*, while the spacing between the two twins is kept constant at $\boldsymbol{s} = 100$ voxels. Both twins are introduced simultaneously after initial compression following the procedure for two-twin FFT simulation presented in Ref. [50]. After twinning, the TRSS distribution in the twin's domain is shown in Fig. 13b, for the case $r = 200$ voxels. From the TRSS distribution, we observe that the stress reversal is severe in the twin that is closer to the hard surface (twin-2) compared to the other one (twin-1). To

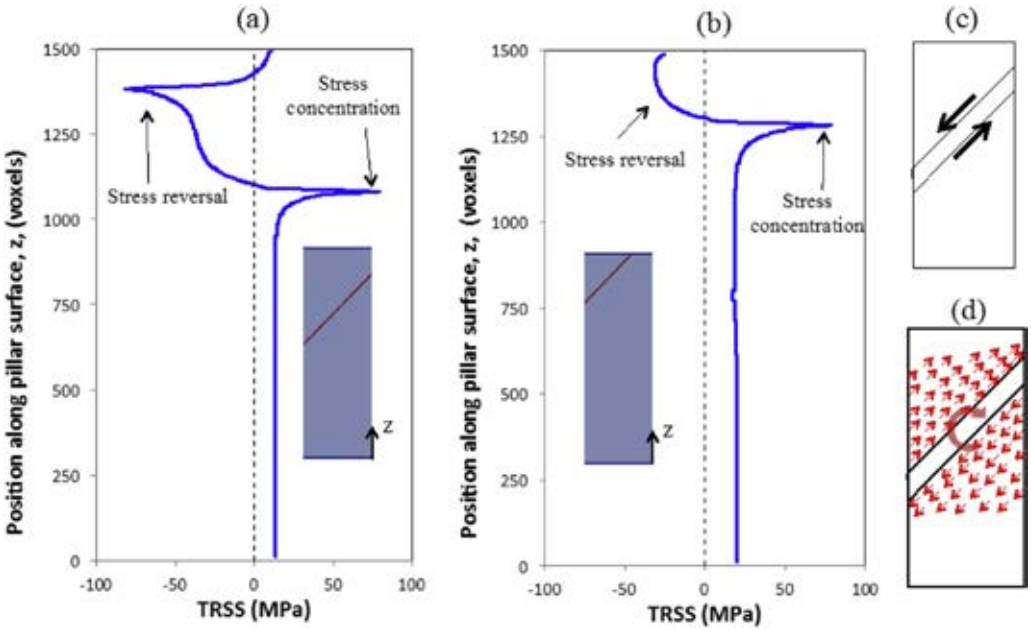

Fig. 12. TRSS profile along the right pillar surface for: (a) free surface case, and (b) 'hard' surface case. The profile shows a stress concentration in both cases that may act as a stress riser for the nucleation of another twin. (c–d) Schematic representation to explain and connect the local mechanics associated with twinning shear and the observed stress concentration in pillar surface. Black arrows in (c) represent twinning shear direction, and all red arrows in (d) represent stress reversal direction. (For interpretation of the references to colour in this figure legend, the reader is referred to the web version of this article.)

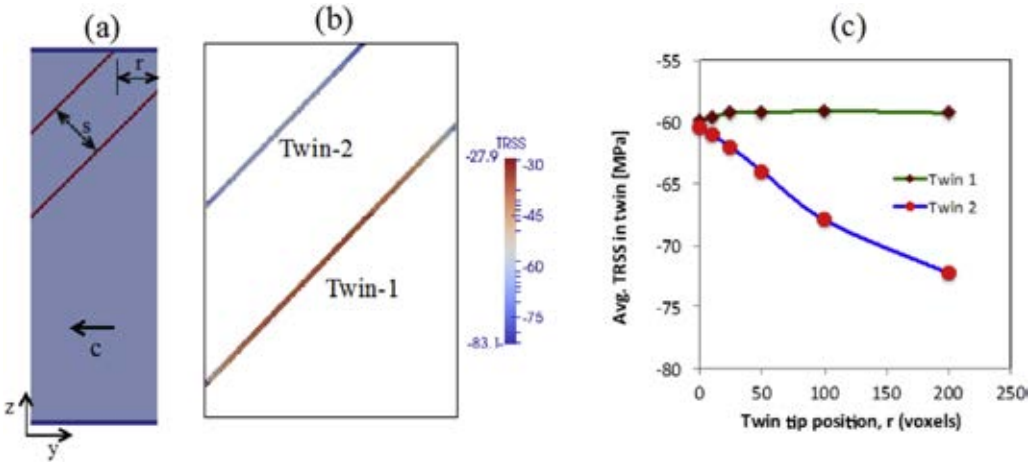

Fig. 13. (a) Schematic representation of the FFT simulation setup with two twins characterized by r and s. (b) TRSS distribution in twin-1 and twin-2. The stress heterogeneity within each twin and the stress difference between the twins is induced by the twinning shear and its accommodation by the surrounding material under the load-displacement boundary conditions. (c) Average TRSS in both twins as a function of position, **r**.

make it more quantitative, the average TRSS in twin-1 and twin-2 is presented as a function of ***r*** in Fig. 13c. It shows that the average TRSS is negative in both twins for all ***r***-values. But the average TRSS is relatively higher in twin-1 compared to twin-2. Moreover, the variation in average TRSS with ***r***-value is significant for twin-2 and negligible for twin-1. The larger stress reversal in twin-2 is due to less plastic accommodation by the presence of the hard phase compared to twin-1. This average TRSS analysis explains why twin-1 is more likely to grow compared to twin-2 under further compression.

4. Conclusions

In summary, we have used *in situ* SEM micropillar compression to examine the critical stress associated with basal slip and twinning in single-crystal magnesium with and without pre-existing $\{01\bar{1}2\}$ deformation twins. Our results show that micropillars with 10 μm diameters are representative of the mechanical response of bulk single crystal samples. The critical compressive stresses for twin growth and basal slip were then measured as 60 MPa and 12 MPa, corresponding to critical resolved shear stresses of 29 MPa and 6 MPa, respectively. Moreover, our results suggest that when using micropillar experiments for twinning characterization one should make sure that the twinning features being analyzed should not be close to the hard indenter surface in order to avoid local stress effects. This study provides a validated methodology on exploring mechanical and materials responses on magnesium with complex microstructures by using micropillar compression techniques.

Acknowledgements

Y.L, M.A.K, R.J.M, C.N.T acknowledge support by the Office of Basic Energy Sciences, Project FWP 06SCPE401, under US DOE Contract No W-7405-ENG-36. J.W acknowledges support by the US National Science Foundation (NSF-CMMI) under grant No.1661686. The authors acknowledge the single-crystal magnesium preparation done by Prof. Y. Jiang and Dr. Q. Yu at University of Nevada, Reno, under Contract FEIN #886000024, and Dr. R.A. Lebensohn (MST-8, Los Alamos National Laboratory) for making available the EVPFFT code used for the numerical simulations. This work was performed, in part, at the Center for Integrated Nanotechnologies, an Office of Science User Facility operated for the U.S. Department of Energy (DOE) Office of Science. Los Alamos National Laboratory, an affirmative action equal opportunity employer, is operated by Los Alamos National Security, LLC, for the National Nuclear Security Administration of the U.S. Department of Energy under contract DE-AC52-06NA25396. The research was performed in part in the Nebraska Nanoscale Facility: National Nanotechnology Coordinated Infrastructure and the Nebraska Center for Materials and Nanoscience, which are supported by the National Science Foundation under Award ECCS: 1542182, and the Nebraska Research Initiative. Access to microscopy facilities at the Electron Microscopy Lab at Los Alamos National Laboratories is also acknowledged.

Appendix A. Supplementary data

Supplementary data related to this article can be found at http://dx.doi.org/10.1016/j.actamat.2017.06.008.

References

[1] M.K. Kulekci, Magnesium and its alloys applications in automotive industry, Int. J. Adv. Manuf. Technol. 39 (2008) 851–865.
[2] P.G. Partridge, The crystallography and deformation modes of hexagonal close-packed metals, Metall. Rev. 12 (1967) 169–194.
[3] M. Yoo, Slip, twinning, and fracture in hexagonal close-packed metals, Metall. Trans. A 12 (1981) 409–418.
[4] J.W. Christian, S. Mahajan, Deformation twinning, Progr Mater. Sci. 39 (1995) 1–157.
[5] A. Serra, D.J. Bacon, R.C. Pond, Dislocations in interfaces in the hcp metals—I. Defects formed by absorption of crystal dislocations, Acta Mater. 47 (1999) 1425–1439.
[6] M.R. Barnett, Twinning and the ductility of magnesium alloys: Part I: "Tension" twins, Mater. Sci. Eng. A 464 (2007) 1–7.
[7] X.Y. Lou, M. Li, R.K. Boger, S.R. Agnew, R.H. Wagoner, Hardening evolution of AZ31B Mg sheet, Int. J. Plast. 23 (2007) 44–86.
[8] I.J. Beyerlein, L. Capolungo, P.E. Marshall, R.J. McCabe, C.N. Tomé, Statistical analyses of deformation twinning in magnesium, Phil. Mag. 90 (2010) 2161–2190.
[9] B.Y. Liu, J. Wang, B. Li, L. Lu, X.Y. Zhang, Z.W. Shan, J. Li, C.L. Jia, J. Sun, E. Ma, Twinning-like lattice reorientation without a crystallographic twinning plane, Nat. Commun. 5 (2014) 3297.
[10] L. Wu, A. Jain, D.W. Brown, G.M. Stoica, S.R. Agnew, B. Clausen, D.E. Fielden, P.K. Liaw, Twinning–detwinning behavior during the strain-controlled low-cycle fatigue testing of a wrought magnesium alloy, ZK60A, Acta Mater. 56 (2008) 688–695.
[11] J. Wang, J.P. Hirth, C.N. Tomé, (10–12) twinning nucleation mechanisms in hexagonal-close-packed crystals, Acta Mater. 57 (2009) 5521–5530.
[12] L. Wang, P. Eisenlohr, Y. Yang, T.R. Bieler, M.A. Crimp, Nucleation of paired twins at grain boundaries in titanium, Scr. Mater. 63 (2010) 827–830.
[13] J. Wang, I.J. Beyerlein, C.N. Tomé, An atomic and probabilistic perspective on twin nucleation in Mg, Scr. Mater. 63 (2010) 741–746.
[14] J.F. Nie, Y.M. Zhu, J.Z. Liu, X.Y. Fang, Periodic segregation of solute atoms in fully coherent twin boundaries, Science 340 (2013) 957–960.
[15] H. Wang, P.D. Wu, J. Wang, C.N. Tomé, A crystal plasticity model for hexagonal close packed (HCP) crystals including twinning and de-twinning mechanisms, Int. J. Plast. 49 (2013) 36–52.
[16] B.M. Morrow, R.J. McCabe, E.K. Cerreta, C.N. Tomé, In-situ TEM observation of twinning and detwinning during cyclic loading in Mg, Metall. Mater. Trans. A 45 (2014) 36–40.
[17] C.D. Barrett, H. El Kadiri, Impact of deformation faceting on and embryonic twin nucleation in hexagonal close-packed metals, Acta Mater. 70 (2014) 137–161.
[18] Y. Liu, N. Li, S. Shao, M. Gong, J. Wang, R. McCabe, Y. Jiang, C. Tomé, Characterizing the boundary lateral to the shear direction of deformation twins in magnesium, Nat. Commun. 7 (2016) 11577.
[19] Q. Yu, J. Wang, Y. Jiang, R.J. McCabe, N. Li, C.N. Tomé, Twin–twin interactions in magnesium, Acta Mater. 77 (2014) 28–42.
[20] Q. Yu, J. Wang, Y. Jiang, Inverse slip accompanying twinning and detwinning during cyclic loading of magnesium single crystal, J. Mater. 2013 (2013) 903786.
[21] Q. Yu, J. Wang, Y. Jiang, R.J. McCabe, C.N. Tomé, Co-zone {-1012} twin interaction in magnesium single crystal, Mater. Res. Lett. 2 (2014) 82–88.
[22] B.M. Morrow, E.K. Cerreta, R.J. McCabe, C.N. Tomé, Toward understanding twin–twin interactions in hcp metals: utilizing multiscale techniques to characterize deformation mechanisms in magnesium, Mater. Sci. Eng. A 613 (2014) 365–371.
[23] P.A. Juan, C. Pradalier, S. Berbenni, R.J. McCabe, C.N. Tomé, L. Capolungo, A statistical analysis of the influence of microstructure and twin–twin junctions on twin nucleation and twin growth in Zr, Acta Mater. 95 (2015) 399–410.
[24] M.D. Uchic, D.M. Dimiduk, J.N. Florando, W.D. Nix, Sample dimensions influence strength and crystal plasticity, Science 305 (2004) 986–989.
[25] N.A. Mara, D. Bhattacharyya, P. Dickerson, R.G. Hoagland, A. Misra, Deformability of ultrahigh strength 5 nm Cu/Nb nanolayered composites, Appl. Phys. Lett. 92 (2008) 231901.
[26] J. San Juan, M.L. Nó, C.A. Schuh, Superelasticity and shape memory in micro- and nanometer-scale pillars, Adv. Mater. 20 (2008) 272–278.
[27] M.D. Uchic, P.A. Shade, D.M. Dimiduk, Plasticity of micrometer-scale single crystals in compression, Annu. Rev. Mater. Res. 39 (2009) 361–386.
[28] J.R. Greer, J.T.M. De Hosson, Plasticity in small-sized metallic systems: intrinsic versus extrinsic size effect, Progr Mater. Sci. 56 (2011) 654–724.
[29] E. Husser, E. Lilleodden, S. Bargmann, Computational modeling of intrinsically induced strain gradients during compression of c-axis-oriented magnesium single crystal, Acta Mater. 71 (2014) 206–219.
[30] J.P. Hirth, J. Lothe, Theory of Dislocations, Wiley, New York, 1982.
[31] J.R. Greer, W.C. Oliver, W.D. Nix, Size dependence of mechanical properties of gold at the micron scale in the absence of strain gradients, Acta Mater. 53 (2005) 1821–1830.
[32] A. Misra, J.P. Hirth, R.G. Hoagland, Length-scale-dependent deformation mechanisms in incoherent metallic multilayered composites, Acta Mater. 53 (2005) 4817–4824.
[33] A.A. Benzerga, N.F. Shaver, Scale dependence of mechanical properties of single crystals under uniform deformation, Scr. Mater. 54 (2006) 1937–1941.
[34] C.A. Volkert, E.T. Lilleodden, Size effects in the deformation of sub-micron Au columns, Phil. Mag. 86 (2006) 5567–5579.
[35] L. Lu, X. Chen, X. Huang, K. Lu, Revealing the maximum strength in nanotwinned copper, Science 323 (2009) 607–610.
[36] Q. Yu, Z.W. Shan, J. Li, X. Huang, L. Xiao, J. Sun, E. Ma, Strong crystal size effect on deformation twinning, Nature 463 (2010) 335–338.
[37] J.Y. Zhang, S. Lei, Y. Liu, J.J. Niu, Y. Chen, G. Liu, X. Zhang, J. Sun, Length scale-dependent deformation behavior of nanolayered Cu/Zr micropillars, Acta Mater. 60 (2012) 1610–1622.
[38] N. Ozdemir, I. Karaman, N.A. Mara, Y.I. Chumlyakov, H.E. Karaca, Size effects in the superelastic response of Ni54Fe19Ga27 shape memory alloy pillars with a two stage martensitic transformation, Acta Mater. 60 (2012) 5670–5685.
[39] E.W. Kelly, W.F. Hosford, Plane-strain compression of magnesium and magnesium alloy crystals, Trans. Metall. Soc. AIME 242 (1968) 5–13.
[40] Q. Yu, L. Qi, R.K. Mishra, J. Li, A.M. Minor, Reducing deformation anisotropy to achieve ultrahigh strength and ductility in Mg at the nanoscale, Proc. Natl. Acad. Sci. 110 (2013) 13289–13293.
[41] J. Ye, R.K. Mishra, A.K. Sachdev, A.M. Minor, In situ TEM compression testing of Mg and Mg–0.2 wt.% Ce single crystals, Scr. Mater. 64 (2011) 292–295.
[42] C.M. Byer, K. Ramesh, Effects of the initial dislocation density on size effects in single-crystal magnesium, Acta Mater. 61 (2013) 3808–3818.
[43] K.E. Prasad, K. Rajesh, U. Ramamurty, Micropillar and macropillar compression responses of magnesium single crystals oriented for single slip or extension twinning, Acta Mater. 65 (2014) 316–325.
[44] A. Budiman, K.R. Narayanan, N. Li, J. Wang, N. Tamura, M. Kunz, A. Misra, Plasticity evolution in nanoscale Cu/Nb single-crystal multilayers as revealed by synchrotron X-ray microdiffraction, Mater. Sci. Eng. A 635 (2015) 6–12.
[45] Q. Yu, L. Qi, K. Chen, R.K. Mishra, J. Li, A.M. Minor, The nanostructured origin of deformation twinning, Nano Lett. 12 (2012) 887–892.
[46] X. Liao, J. Wang, J. Nie, Y. Jiang, P. Wu, Deformation twinning in hexagonal materials, MRS Bull. 41 (2016) 314–319.
[47] J. Hirth, J. Wang, C. Tomé, Disconnections and other defects associated with twin interfaces, Progr Mater. Sci. 83 (2016) 417–471.
[48] R.C. Pond, J. Hirth, A. Serra, D. Bacon, Atomic displacements accompanying deformation twinning: shears and shuffles, Mater. Res. Lett. 4 (2016) 185–190.
[49] M. Arul Kumar, A.K. Kanjarla, S.R. Niezgoda, R.A. Lebensohn, C.N. Tomé, Numerical study of the stress state of a deformation twin in magnesium, Acta Mater. 84 (2015) 349–358.
[50] M. Arul Kumar, I.J. Beyerlein, C.N. Tomé, Effect of local stress fields on twin characteristics in HCP metals, Acta Mater. 116 (2016) 143–154.